Array-Aided GNSS for Precise Determination of Ionospheric and Tropospheric Delays With Integer Ambiguity Resolution

Xingyu Chen, Xiaolong Mi, Yunbin Yuan, Ahmed El-Mowafy, Hongjin Xu, and Wenwu Ding

***Abstract*— Ground-based global navigation satellite system (GNSS) observations are essential for acquiring high-precision ionospheric and tropospheric information due to their superior temporal and spatial resolution, making them invaluable in space weather monitoring and meteorology. However, the widely used single-station precise point positioning (PPP) technology faces accuracy challenges due to the need to estimate a large number of parameters and the presence of float ambiguities. Array-aided GNSS technology holds promise for enhancing atmospheric information extraction through redundant observations. Yet, traditional array-aided models struggle to extract tropospheric delays, as tropospheric parameters are absorbed by satellite clocks during the elimination of rank deficiencies. In this article, we present an array-aided precise atmospheric delay determination (A-PADD) method that incorporates integer ambiguity resolution (IAR). Building on the PPP framework, we develop a full-rank model that allows for the simultaneous estimation of ionospheric and tropospheric parameters, utilizing a short baseline for rapid IAR. Through canonical decomposition (CD) theory, we analytically demonstrate that while IAR does not enhance ionospheric delay estimation, it improves the determination of tropospheric delays. Empirical data corroborate this theoretical insight. Our experimental results show that the A-PADD method surpasses the traditional PPP method in terms of accuracy and stability of atmospheric delay extraction. Specifically, for ionospheric delay determination, A-PADD accelerates the initialization process through additional redundant observations. For tropospheric delay determination, A-PADD improves the extraction accuracy by 23% compared to traditional PPP and shows greater consistency with the international GNSS service (IGS) final product. Therefore, within the array-aided framework, for applications solely focused on ionospheric delay estimation, higher accuracy can be achieved without IAR, thereby reducing computational requirements. For applications requiring both ionospheric and tropospheric delay information, implementing IAR is advantageous, particularly during the initialization phase of tropospheric delay determination.**

***Index Terms*— Array-aided precise atmospheric delays determination (A-PADD), canonical decomposition (CD), global navigation satellite systems (GNSSs), integer ambiguity resolution (IAR), ionospheric delay, tropospheric delay.**

I. Introduction

THE ionosphere, a critical component of space weather, is predominantly formed by the Sun's high-energy electromagnetic and particle radiation and its variations. Despite significant advancements, the intricate coupling processes within the ionosphere remain incompletely understood, necessitating further investigation [1]. Additionally, the ionosphere's influence on contemporary technologies, such as communication, navigation, and remote sensing, demands continuous and reliable monitoring and forecasting to mitigate potential disruptions, particularly during space weather events such as solar flares [2], [3], [4], [5], [6] and coronal mass ejections [7], [8].

Similarly, the troposphere, the lowest layer of the Earth's atmosphere, containing approximately 80% of the atmospheric mass and 99% of the water vapor and aerosols, plays a pivotal role in weather and climate dynamics [9]. Most weather phenomena occur within the troposphere, making it a primary focus for atmospheric studies. Zenith tropospheric delay (ZTD) is a crucial input parameter for numerical weather prediction models [10], [11], [12], enhancing the accuracy of weather forecasts. Additionally, zenith wet delay (ZWD) is strongly correlated with precipitable water vapor (PWV), making it valuable for studies on water vapor monitoring and climate change [13], [14], [15].

Accurate detection and monitoring of the Earth's ionosphere and troposphere are therefore essential for understanding atmospheric processes and improving weather prediction models. Various observational technologies have been developed for this purpose, each with its unique strengths and limitations. For ionospheric total electron content (TEC) detection, altimeters and incoherent scatter radars are commonly used. Altimeters measure the height of the ionosphere

Received 28 August 2024; revised 20 November 2024, 8 January 2025, and 1 April 2025; accepted 14 April 2025. Date of publication 18 April 2025; date of current version 30 April 2025. This work was supported in part by the National Natural Science Foundation of China under Grant 42404052 and Grant 42374043, in part by the Key Research and Development Plan of Hubei Province under Grant 2021EHB001, in part by the Youth Innovation Promotion Association Chinese Academy of Sciences (CAS), and in part by the National Key Research Program of China under Grant 2016YFB0501900. *(Corresponding author: Xiaolong Mi.)*

Xingyu Chen is with the Innovation Academy for Precision Measurement Science and Technology, Chinese Academy of Sciences, Wuhan 430077, China, and also with the College of Earth and Planetary Sciences, University of Chinese Academy of Sciences, Beijing 100049, China (e-mail: xingyu-max.chen@polyu.edu.hk).

Xiaolong Mi is with the Department of Land Surveying and Geo-Informatics, The Hong Kong Polytechnic University, Hong Kong (e-mail: xiaolong.mi@polyu.edu.hk).

Yunbin Yuan, Hongjin Xu, and Wenwu Ding are with the Innovation Academy for Precision Measurement Science and Technology, Chinese Academy of Sciences, Wuhan 430077, China (e-mail: yybgps@asch.whigg.ac.cn; xuhongjin@asch.whigg.ac.cn; dingwenwu@apm.ac.cn).

Ahmed El-Mowafy is with the School of Earth and Planetary Sciences, Curtin University, Perth, WA 6102, Australia (e-mail: A.El-Mowafy@curtin.edu.au).

Digital Object Identifier 10.1109/TGRS.2025.3562224

by bouncing radio waves off its layers, while incoherent scatter radars provide detailed profiles of electron density by scattering radio waves off free electrons [16], [17]. For tropospheric water vapor extraction, microwave radiometers (MWRs) are widely employed. MWRs measure the intensity of microwave radiation emitted by atmospheric water vapor, providing valuable data on water vapor content [18]. Despite the effectiveness of these technologies, global navigation satellite system (GNSS) offers several advantages that make them superior for atmospheric observation. GNSS provides continuous, high-resolution data with extensive spatial and temporal coverage. Ground-based GNSS receivers can accurately determine ZTDs and extract TEC from ionospheric observations, making GNSS a versatile tool for atmospheric research [19], [20], [21], [22], [23].

Precise point positioning (PPP) has been widely adopted in GNSS for ionosphere and troposphere detection. Utilizing precise satellite clock and orbit products released by the international GNSS service (IGS) and employing the undifferenced (UD) uncombined PPP (UCPPP) model, both ionospheric and tropospheric delays can be estimated, retaining all observational information and facilitating extension to multifrequency observations [24], [25]. However, in real-world GNSS observations, PPP has certain limitations for extracting atmospheric delays. First, the parameter estimation process is complex and challenging, often requiring a long convergence time (CVT). Additionally, the model strength of single-station observations is weak and susceptible to interference from instrumentation and environment such as in low SNR scenarios or in the presence of wideband interferences [26]. Furthermore, since the ambiguities are not fixed, the estimates of atmospheric parameters cannot achieve the theoretically optimal accuracy.

Our study is motivated by the underutilization of data from continuously operating reference stations (CORSs), which often have multiple receivers to maintain spatial reference frameworks and monitor positioning service integrity [27], [28]. These colocated data, available within very short distances, offer an opportunity to enhance parameters estimation by improving model robustness and reducing observational noise. Building on this, the concept of array-aided GNSS has been successfully applied in various fields, such as attitude determination, high-performance positioning [29], [30], [31], [32], and mitigating receiver spoofing and environmental interference like multipath effects [33], [34], [35].

Extending array-aided GNSS concept to atmospheric monitoring has shown both potential and limitations in previous research. For example, Zaminpardaz et al. [36] and Khodabandeh and Teunissen [37] applied the satellite clock estimated (SCE) model, based on broadcast ephemeris, to improve ionospheric delay extraction. Despite its benefits, this model, derived from UD RTK, cannot directly estimate ZTD at a single station. This limitation arises because tropospheric parameters are absorbed into the satellite clock estimates to eliminate rank deficiencies, thus constraining its use in meteorological applications. In contrast, Wang et al. [38] used the UCPPP model to reorganize atmospheric parameters for tropospheric delay estimation with low-cost receivers, but it did not address ionospheric delays or achieve integer ambiguity resolution (IAR), thus not reaching optimal theoretical accuracy.

Our contribution enhances the array-aided GNSS framework by introducing the satellite clock fixed (SCF) model [39], [40], which leverages external precise satellite clock products to enable the direct estimation of both ionospheric and tropospheric delays. We successfully implement IAR and provide a comprehensive theoretical and experimental analysis of the benefits of array-aided GNSS in atmospheric delay estimation. Our work evaluates the impact of IAR on atmospheric parameter estimation and offers practical guidance for its implementation, enhancing the efficiency and accuracy of atmospheric monitoring.

In Section II, we first outline the GNSS raw carrier phase and pseudorange equations, introduce the UCPPP observation model, and present the array-aided precise atmospheric delay determination (A-PADD) concept, along with its mathematical model incorporating IAR. We extend the canonical decomposition (CD) theory from the SCE model to the SCF model, partitioning atmospheric parameters into UD, between-station single-differenced (SD), between-satellite SD, and double-differenced (DD) components. This theoretical framework supports our experimental evaluation of IAR's influence on atmospheric parameter accuracy and the comparative performance of UCPPP and A-PADD.

II. Ionospheric and Tropospheric Delays Estimation

A. GNSS Raw Observation Equations

The phase and pseudorange observations of GNSS are the fundamental data for this study, so the UD and uncombined GNSS observations are first introduced. We assume that at epoch i, receiver $r = 1, \ldots, n$ simultaneously tracks the satellite $s = 1, \ldots, m$ at the $j = 1, \ldots, f$ frequency. The expression can be written as follows [41]:

$$\begin{aligned} E\left(\Delta p^s_{r,j}(i)\right) &= \rho^s_r(i) + m^s_r(i)\cdot\tau_r(i) + dt_r(i) - dt^s(i) \\ &\quad + \mu_j \iota^s_r(i) + d_{r,j} - d^s_{,j} \\ E\left(\Delta \phi^s_{r,j}(i)\right) &= \rho^s_r(i) + m^s_r(i)\cdot\tau_r(i) + dt_r(i) - dt^s(i) \\ &\quad - \mu_j \iota^s_r(i) + \delta_{r,j} - \delta^s_{,j} + \lambda_j z^s_{r,j} \end{aligned} \tag{1}$$

where $E(\cdot)$ represents the mathematical expectation operator and $\Delta p^s_{r,j}(i)$ and $\Delta \phi^s_{r,j}(i)$ denote the code and phase observations minus the computed values (O–C), respectively. The empirical tropospheric dry delay, phase wrapping effect, tidal effect, and satellite and receiver antenna phase center offset (PCO) and phase center variation (PCV) are corrected in the above observations, i.e., the observations are reduced from these errors. The parameter $\rho^s_r(i) = g^s_r(i)\cdot\Delta x_r(i)$ represents the geometric distance correction term in the station-to-satellite line-of-sight direction. In this context, $g^s_r(i)$ is a 1×3 vector representing the unit vector in the satellite-receiver line-of-sight direction; $\Delta x_r(i)$ is a 3×1 vector representing the increments of position; $m^s_r(i)$ is the tropospheric mapping function; $\tau_r(i)$ denotes the unknown tropospheric wet delay parameter; $dt_r(i)$ and $dt^s(i)$ represent the receiver clock bias and satellite clock bias, respectively; $\iota^s_r(i)$ is the ionospheric slant delay, with its corresponding

TABLE I
UNKNOWN PARAMETERS AND THEIR ESTIMABLE FORMS IN THE UNCOMBINED PPP MODEL

Parameter	Notation and interpretation
S-basis parameters	$d_{r,j}, \delta_{r,j}, d_{r,IF}, z^s_{r,j}, d_{r,GF}, d^s_{,GF}$
Receiver clock bias	$\tilde{dt}_r = dt_r + d_{r,IF}$
Ionospheric delay	$\tilde{I}^s_r = I^s_r + d_{r,GF} - d^s_{,GF}$
Satellite code biases	$\tilde{d}^s_{r,j} = d^s_{,j} - d^s_{,IF} - \mu_j d^s_{,GF} - d_{r,j} + d_{r,IF} + \mu_j d_{r,GF}, \quad j \geq 3$
PPP float ambiguity	$\tilde{\delta}^s_{r,j} = \delta^s_{,j} - d^s_{,IF} + \mu_j d^s_{,GF} - \lambda_j z^s_{r,j} - \delta_{r,j} + d_{r,IF} - \mu_j d_{r,GF}, \quad j \geq 1$

frequency-dependent coefficient defined as $\mu_j = (\lambda_j^2/\lambda_1^2)$; $\lambda_j = c/f_j$ represents the wavelength; c represents the speed of light; the receiver code bias and phase bias are defined as $d_{r,j}$ and $\delta_{r,j}$, respectively; the satellite code bias and phase bias are defined as d^s_j and δ^s_j, respectively; and the ambiguity, in cycles, is defined as $z^s_{r,j}$.

B. Uncombined PPP Model

Due to the coupling of parameters, the design matrix in (1) is rank-deficient. This implies that not all unknown parameters in (1) can be estimated without biases, and only certain combinations of parameters can be accurately estimated [42], [43]. Here, we apply the *S*-basis theory, selecting a number of parameters equal to the rank deficiency as the *S*-basis, reprocessing the parameters to obtain their linearly estimable forms, and ultimately forming a full-rank design matrix [44]. To realize monitoring of the ionosphere and troposphere, their parameters must be present after eliminating the rank deficiencies, and hence, the uncombined PPP form is the only choice. By introducing IGS precise satellite orbit and clock products and eliminating the rank deficiencies, the full-rank uncombined PPP model can be expressed as [45]

$$\begin{aligned} &E\left(\Delta\tilde{p}^s_{r,j}(i)\right) \\ &\quad = \rho^s_r(i) + m^s_r(i)\cdot\tau_r(i) + d\tilde{t}_r(i) + \mu_j\tilde{\imath}^s_r(i) - \tilde{d}^s_{r,j} \\ &E\left(\Delta\tilde{\phi}^s_{r,j}(i)\right) \\ &\quad = \rho^s_r(i) + m^s_r(i)\cdot\tau_r(i) + d\tilde{t}_r(i) - \mu_j\tilde{\imath}^s_r(i) - \tilde{\delta}^s_{r,j} \end{aligned} \tag{2}$$

where the O–C observations $\Delta\tilde{p}^s_{r,j}(i) = \Delta p^s_{r,j}(i) + d\tilde{t}^s$ and $\Delta\tilde{\phi}^s_{r,j}(i) = \Delta\phi^s_{r,j}(i) + d\tilde{t}^s$, with $d\tilde{t}^s = dt^s + d^s_{,\mathrm{IF}}$ representing the introduced IGS precise satellite clock products. The tilde symbol ($\tilde{}$) denotes the reprocessed estimable form. Table I shows the estimable forms and definitions of each parameter. The geometry-free combination $(\cdot)_{,\mathrm{GF}}$ and the ionosphere-free combination $(\cdot)_{,\mathrm{IF}}$ are defined as follows [46]:

$$\begin{aligned} (\cdot)_{,\mathrm{GF}} &= \frac{1}{\mu_2-\mu_1}(\cdot)_2 - \frac{1}{\mu_2-\mu_1}(\cdot)_1 \\ (\cdot)_{,\mathrm{IF}} &= \frac{\mu_2}{\mu_2-\mu_1}(\cdot)_2 - \frac{\mu_1}{\mu_2-\mu_1}(\cdot)_1 \end{aligned} \tag{3}$$

where $(\cdot)_{j=1,2}$ denotes the corresponding frequency.

Using the model provided in (2) and Table I, the ionospheric observations can be easily determined and used as input for ionospheric models such as the GIM, after correctly processing differential code biases (DCBs) [37]. Additionally, the tropospheric wet delay can be extracted for use in water vapor monitoring.

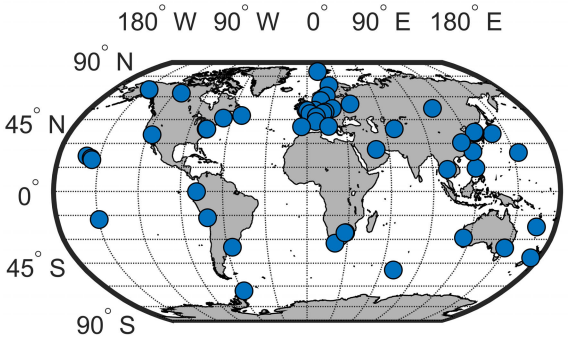

Fig. 1. Global distribution of colocated reference stations in IGS network (i.e., equipped with two or more receivers located a few meters to hundreds of meters apart).

C. Array-Aided Precise Atmospheric Delays Determination (A-PADD)

As shown in Table I, the final form of the UCPPP ambiguity remains a float solution. This limitation prevents the effective use of the integer nature of DD ambiguity, which could otherwise improve the estimation of other parameters.

For the construction and maintenance of CORS, some stations are typically equipped with two or more receivers and antennas. Fig. 1 shows the distribution of colocated receivers in the IGS network. As of July 2024, colocated reference stations account for 22% of the total number of reference stations, with a relatively uniform global distribution. Under the hardware configuration, the concept of array-aided GNSS can be applied, which can enhance the estimability of GNSS parameters, such as position, attitude, and clock bias. The traditional array-aided GNSS model, based on SCE method, can be expressed as follows:

$$\begin{aligned} E\left(\Delta\tilde{p}^s_{1,j}(i)\right) &= \rho^s_1(i) - d\tilde{t}^s(i) + \mu_j\tilde{\imath}^s_1(i) - \tilde{d}^s_{1,j} \\ E\left(\Delta\tilde{\phi}^s_{1,j}(i)\right) &= \rho^s_1(i) - d\tilde{t}^s(i) - \mu_j\tilde{\imath}^s_1(i) - \tilde{\delta}^s_{1,j} \\ E\left(\Delta\tilde{p}^s_{2,j}(i)\right) &= \rho^s_2(i) - d\tilde{t}^s(i) + d\tilde{t}_{12}(i) + m^s_2(i)\cdot\tau_{12}(i) \\ &\quad + d\tilde{t}_2(i) + \mu_j\tilde{\imath}^s_1(i) \\ &\quad + \mu_j d_{12,\mathrm{GF}} - \tilde{d}^s_{1,j} + \tilde{d}_{12,j} \end{aligned}$$

TABLE II
SCF MODEL UNKNOWN PARAMETERS AND THEIR ESTIMABLE FORMS

Parameter	Notation and interpretation
S-basis parameters	$\tilde{d}_{1,j}, \tilde{\delta}_{1,j}, z^{s}_{12,j}$
Between-receiver code bias	$\tilde{d}_{12,j} = d_{2,j} - d_{1,j} - d_{12,IF} - \mu_j d_{12,GF}, \quad j \geq 3$
Between-receiver phase bias	$\tilde{\delta}_{12,j} = \delta_{2,j} - \delta_{1,j} - d_{12,IF} + \mu_j d_{12,GF} + \lambda_j N^{1}_{12,j}$ $j \geq 1$
DD Ambiguity	$z^{1s}_{12,j} = z^{s}_{12,j} - z^{1}_{12,j}, \quad s \geq 1, \quad j \geq 1$

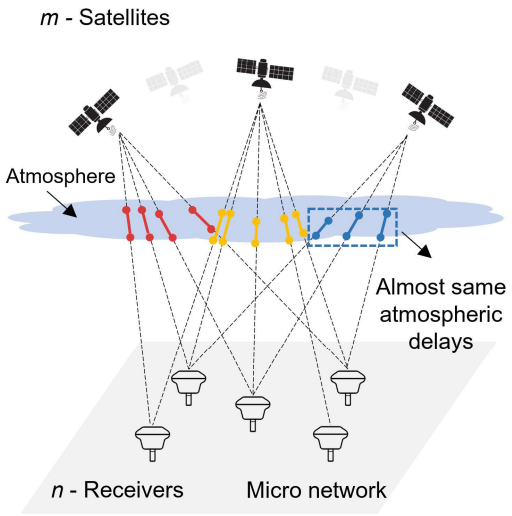

Fig. 2. Principle of A-PADD.

$$E\left(\Delta\tilde{\phi}^{s}_{2,j}(i)\right) = \rho^{s}_{2}(i) - d\tilde{\tilde{t}}^{s}(i) + d\tilde{t}_{12}(i) + m^{s}_{2}(i)\cdot\tau_{12}(i) + d\tilde{t}_{2}(i) - \mu_j \tilde{\imath}^{s}_{1}(i) - \mu_j d_{12,\mathrm{GF}} - \tilde{\delta}^{s}_{1,j} + \tilde{\delta}_{12,j} + \lambda_j z^{1s}_{12,j} \quad (4)$$

where $d\tilde{\tilde{t}}^{s}(i) = dt^{s}(i) - dt_1(i) + d^{s}_{,\mathrm{IF}} - d_{A,\mathrm{IF}} - m^{s}_{1}(i)\tau_1(i)$, $d\tilde{t}_{12}(i) = dt_{12}(i) + d_{12,\mathrm{IF}}$, $\tau_{12} = \tau_1 - \tau_2$, and the other estimable forms are presented in Table II.

As shown in (4), the estimated satellite clock bias absorbs tropospheric delays, thereby preventing the direct estimation of ZTD at a single station. To further improve the performance of atmospheric delay determination in both ionosphere and troposphere, we incorporate external satellite clock products into the array-aided GNSS framework and use the SCF model to enhance robustness. Fig. 2 illustrates the principle of A-PADD. In a micronetwork with ultrashort baselines (or zero baselines) between receivers, the satellite signal propagation paths are nearly identical, resulting in very similar atmospheric conditions. As a result, the functional model can be improved concerning three key aspects: first, by using the nearly identical atmospheric conditions to estimate unified parameters and increase redundant observations, thereby strengthening the model; second, by incorporating precise satellite orbits and clock products, which enable the direct estimation of ionospheric and tropospheric delays at single stations; and third, by utilizing the short baselines to facilitate IAR at the colocated stations, enabling rapid IAR, leading to high-precision atmospheric delay determination.

Starting from (2), assume that atmospheric delays are extracted from two stations 1 and 2 (with Station 1 as the reference station) in a micronetwork. The satellite code biases $d^{s}_{,j} - d^{s}_{,\mathrm{IF}} - \mu_j d^{s}_{,\mathrm{GF}}$ and phase biases $\delta^{s}_{,j} - d^{s}_{,\mathrm{IF}} - \mu_j d^{s}_{,\mathrm{GF}}$ are identical at both stations. By using precise satellite clock products, the influence of satellite bias parameters can be eliminated. Furthermore, selecting common parameters as the S-basis allows DD ambiguity parameters with integer characteristics to be obtained, which can be directly used for IAR. This model is referred to as the SCF model and can be expressed as follows [39]:

$$\begin{aligned}
&E\left(\Delta\tilde{p}^{s}_{1,j}(i)\right) \\
&\quad = \rho^{s}_{1}(i) + m^{s}_{1}(i)\cdot\tau_1(i) + d\tilde{t}_1(i) + \mu_j\tilde{\imath}^{s}_{1}(i) - \tilde{d}^{s}_{1,j} \\
&E\left(\Delta\tilde{\phi}^{s}_{1,j}(i)\right) \\
&\quad = \rho^{s}_{1}(i) + m^{s}_{1}(i)\cdot\tau_1(i) + d\tilde{t}_1(i) - \mu_j\tilde{\imath}^{s}_{1}(i) - \tilde{\delta}^{s}_{1,j} \\
&E\left(\Delta\tilde{p}^{s}_{2,j}(i)\right) \\
&\quad = \rho^{s}_{2}(i) + m^{s}_{2}(i)\cdot\tau_2(i) + d\tilde{t}_2(i) + \mu_j\tilde{\imath}^{s}_{2}(i) - \tilde{d}^{s}_{1,j} + \tilde{d}_{12,j} \\
&E\left(\Delta\tilde{\phi}^{s}_{2,j}(i)\right) \\
&\quad = \rho^{s}_{2}(i) + m^{s}_{2}(i)\cdot\tau_2(i) + d\tilde{t}_2(i) - \mu_j\tilde{\imath}^{s}_{2}(i) - \tilde{\delta}^{s}_{1,j} \\
&\qquad + \tilde{\delta}_{12,j} + \lambda_j z^{1s}_{12,j}
\end{aligned} \quad (5)$$

where the estimable forms of the newly introduced parameters are shown in Table II.

In practice, the distance between antenna arrays in A-PADD is typically less than 10 km, resulting in very similar ionospheric delays, where $\tilde{\imath}^{s}_{12} = \tilde{\imath}^{s}_{1} - \tilde{\imath}^{s}_{2} = 0$ [47]. According to Table I, $\tilde{I}^{s}_{1} = I^{s}_{1} + d_{1,\mathrm{GF}} - d^{s}_{,\mathrm{GF}}$, and therefore, $\tilde{I}^{s}_{2} = \tilde{I}^{s}_{1} + d_{12,\mathrm{GF}}$. In summary, the A-PADD model, which utilizes precise clock products and achieves IAR, can be expressed as follows:

$$\begin{aligned}
E\left(\Delta\tilde{p}^{s}_{1,j}(i)\right) &= \rho^{s}_{1}(i) + m^{s}_{1}(i)\cdot\tau_1(i) + d\tilde{t}_1(i) + \mu_j\tilde{\imath}^{s}_{1}(i) - \tilde{d}^{s}_{1,j} \\
E\left(\Delta\tilde{\phi}^{s}_{1,j}(i)\right) &= \rho^{s}_{1}(i) + m^{s}_{1}(i)\cdot\tau_1(i) + d\tilde{t}_1(i) - \mu_j\tilde{\imath}^{s}_{1}(i) - \tilde{\delta}^{s}_{1,j} \\
E\left(\Delta\tilde{p}^{s}_{2,j}(i)\right) &= \rho^{s}_{2}(i) + m^{s}_{2}(i)\cdot\tau_1(i) + d\tilde{t}_2(i) + \mu_j\tilde{\imath}^{s}_{1}(i) + \mu_j d_{12,\mathrm{GF}} - \tilde{d}^{s}_{1,j} + \tilde{d}_{12,j} \\
E\left(\Delta\tilde{\phi}^{s}_{2,j}(i)\right) &= \rho^{s}_{2}(i) + m^{s}_{2}(i)\cdot\tau_1(i) + d\tilde{t}_2(i) - \mu_j\tilde{\imath}^{s}_{1}(i) - \mu_j d_{12,\mathrm{GF}} - \tilde{\delta}^{s}_{1,j} + \tilde{\delta}_{12,j} + \lambda_j z^{1s}_{12,j}.
\end{aligned} \quad (6)$$

Based on (6), the expression for a single receiver pair tracking a single satellite pair can be extended to a multivariate

form. Let us define that receiver r observes m satellites on all frequencies, the phase observation vector can be expressed as $\boldsymbol{\Phi}_r^S = [\boldsymbol{\Phi}_{r,1}^{S^T}, \ldots, \boldsymbol{\Phi}_{r,f}^{S^T}]^T \in \mathbb{R}^{fm}$, where $\boldsymbol{\Phi}_{r,j}^S = [\Delta\phi_{r,j}^1, \ldots, \Delta\phi_{r,j}^m]^T \in \mathbb{R}^m$. For a micronetwork array composed of n receivers, the phase observation matrix can be defined as $\boldsymbol{\Phi}_R^S = [\boldsymbol{\Phi}_1^S, \ldots, \boldsymbol{\Phi}_n^S]^T \in \mathbb{R}^{fm\times n}$, and the code observation matrix can be defined as its counterpart. The full-rank multivariate observation equation corresponding to (6) can then be expressed as

$$\begin{aligned} E\left(\boldsymbol{P}_R^S\right) &= \left[\boldsymbol{e}_f \otimes \boldsymbol{I}_m\right]\boldsymbol{\rho}_R^S + \left[\boldsymbol{e}_f \otimes \boldsymbol{m}_r^S\right] \otimes \boldsymbol{\tau}_R \\ &\quad + \left[\boldsymbol{\mu}_f \otimes \boldsymbol{I}_m\right]\tilde{\boldsymbol{\imath}}_1^S + \left[\boldsymbol{\mu}_f \otimes \boldsymbol{e}_m\right]\tilde{\boldsymbol{d}}_{1R,\mathrm{GF}} \\ &\quad + \left[\boldsymbol{E}_f \otimes \boldsymbol{e}_m\right]\tilde{\boldsymbol{d}}_{1R} - \left[\boldsymbol{E}_f \otimes \boldsymbol{I}_m\right]\tilde{\boldsymbol{d}}_1^S \boldsymbol{e}_n^T \\ E\left(\boldsymbol{\Phi}_R^S\right) &= \left[\boldsymbol{e}_f \otimes \boldsymbol{I}_m\right]\boldsymbol{\rho}_R^S + \left[\boldsymbol{e}_f \otimes \boldsymbol{m}_r^S\right] \otimes \boldsymbol{\tau}_R \\ &\quad - \left[\boldsymbol{\mu}_f \otimes \boldsymbol{I}_m\right]\tilde{\boldsymbol{\imath}}_1^S - \left[\boldsymbol{\mu}_f \otimes \boldsymbol{e}_m\right]\tilde{\boldsymbol{d}}_{1R,\mathrm{GF}} \\ &\quad + \left[\boldsymbol{\Lambda} \otimes \boldsymbol{I}_m\right]\tilde{\boldsymbol{a}}_R^S \end{aligned} \tag{7}$$

where the f-vector $\boldsymbol{e}_f$ contains all elements equal to "one" and $\boldsymbol{I}_m$ is an m-vector identity matrix. The matrix $\boldsymbol{E}_f$ is a $f \times (f-2)$ matrix formed by removing the first two columns of the identity matrix $\boldsymbol{I}_m$. The wavelength matrix is $\boldsymbol{\Lambda} = \mathbf{diag}(\lambda_1, \cdots \lambda_f) \in \mathbb{R}^{f\times f}$. $\otimes$ denotes the Kronecker product. The $m \times n$ geometric distance correction term $\boldsymbol{\rho}_R^S = \boldsymbol{G}\Delta\boldsymbol{x}_R + \boldsymbol{e}_m\boldsymbol{dt}_R$, where $\boldsymbol{G}$ is the geometric matrix composed of unit vectors in the satellite-receiver line-of-sight direction, $\Delta\boldsymbol{x}_R$ is the position increment vector, and $\boldsymbol{dt}_R = [dt_1, \ldots, dt_n] \in \mathbb{R}^{1\times n}$ represents the receivers' clock bias parameters. In a micronetwork where the stations are very close, the unit vectors in the line-of-sight direction of each receiver for the same satellite are almost parallel, making the tropospheric delay mapping function almost the same, i.e., $m_r^s = m_1^s (r = 1, \cdots n)$. Thus, the $m \times 1$ tropospheric mapping function vector $\boldsymbol{m}_r^S = [m_1^1, \ldots, m_1^m]^T$ and the corresponding $1 \times n$ tropospheric wet delay parameters vector $\boldsymbol{\tau}_R = [\tau_1, \ldots, \tau_n]$ can be obtained. The f-vector $\boldsymbol{\mu}_f$ is composed of μ_j, linking the ionospheric delays to the observations. $\tilde{\boldsymbol{d}}_{1*}$ and $\tilde{\boldsymbol{d}}_1^S$ are the code bias correlation matrices, where $\tilde{\boldsymbol{d}}_{1*} = [\boldsymbol{0}, \tilde{\boldsymbol{d}}_{12,,j}, \ldots, \tilde{\boldsymbol{d}}_{1n,,j}](j = 1, \ldots, f)$ and $\tilde{\boldsymbol{d}}^S = [\tilde{\boldsymbol{d}}_{1,3}^{S^T}, \ldots, \tilde{\boldsymbol{d}}_{1,f}^{S^T}]^T (S = 1, \ldots, m)$, which only exist when $f \geq 3$. The ambiguity vector is denoted as $\boldsymbol{a}_R^S$, with its specific expression shown in the following equation following, where $\boldsymbol{\delta}_1^S = [\boldsymbol{\delta}_{1,1}^{S^T}, \ldots, \boldsymbol{\delta}_{1,f}^{S^T}]^T$ and $\boldsymbol{\delta}_{1R} = [\boldsymbol{0}, \boldsymbol{\delta}_{12,j}, \ldots, \boldsymbol{\delta}_{1n,j}]$:

$$\begin{aligned} \boldsymbol{a}_R^S &= \boldsymbol{z}_{1R}^{1S} - \boldsymbol{\Lambda}^-\left(\boldsymbol{\delta}_1^S \boldsymbol{e}_n^T\right) + \boldsymbol{\Lambda}^-\left[\boldsymbol{I}_f \otimes \boldsymbol{e}_m\right]\boldsymbol{\delta}_{1R} \\ \boldsymbol{\Lambda}^- &= \mathbf{diag}\left[\frac{1}{\lambda_1}, \ldots, \frac{1}{\lambda_f}\right]. \end{aligned} \tag{8}$$

The variance–covariance matrix of the observations can be expressed as

$$\begin{aligned} \boldsymbol{Q}_{\boldsymbol{\Phi}_S^R\boldsymbol{\Phi}_S^R} &= \boldsymbol{C}_R \otimes \boldsymbol{C}_\phi \otimes \boldsymbol{C}_s \\ \boldsymbol{Q}_{\boldsymbol{P}_S^R\boldsymbol{P}_S^R} &= \boldsymbol{C}_R \otimes \boldsymbol{C}_P \otimes \boldsymbol{C}_s \end{aligned} \tag{9}$$

where $\boldsymbol{Q}$ represents the variance–covariance matrix; $\boldsymbol{C}_R \in \mathbb{R}^{n\times n}$ is a diagonal matrix, representing the receiver-dependent coefficients, which is an identity matrix when the observation precision of the receivers is the same; $\boldsymbol{C}_{\phi/P} \in \mathbb{R}^{f\times f}$ is the precision matrix for phase and code observations; and $\boldsymbol{C}_s \in \mathbb{R}^{m\times m}$ is the satellite elevation-dependent matrix, with the specific expression given in the following equation, in which E^s is the elevation angle of satellite s:

$$\begin{aligned} \boldsymbol{C}_R &= \begin{bmatrix} c_1^2 & & \\ & \ddots & \\ & & c_n^2 \end{bmatrix}, \quad \boldsymbol{C}_{P/\phi} = \begin{bmatrix} \sigma_{P/\phi,1}^2 & & \\ & \ddots & \\ & & \sigma_{P/\phi,f}^2 \end{bmatrix} \\ \boldsymbol{C}_S &= \begin{bmatrix} c_1^2 & & \\ & \ddots & \\ & & c_m^2 \end{bmatrix}, \quad c_s^2 = \frac{1}{\sin^2(E^s)}. \end{aligned} \tag{10}$$

III. CD and Impact of IAR on Atmospheric Parameters

A. Canonical Decomposition

In (5) and (6), UD and uncombined raw observations are utilized. However, as shown in Table II, the final estimated form of the ambiguity is expressed as DD ambiguities. To better investigate the impact of IAR on atmospheric parameters, the UD model should be decomposed into four uncorrelated blocks: average UD, satellite- and receiver-average SD, and the DD, using a process called CD. This decomposition, originally introduced in [48] and [49], provides a systematic method for separating these components to facilitate better parameter interpretation, as illustrated in (11). The nfm $\times$ nfm multivariate canonical differencing transformation matrix can thus be expressed in the following equation:

$$\mathbf{T}_{\mathrm{CD}}(\cdot)_R^S = \begin{bmatrix} (\cdot)_{\bar{r}}^{\bar{s}} & (\cdot)_{1R}^{\bar{s}} \\ (\cdot)_{\bar{r}}^{1S} & (\cdot)_{1S}^{1R} \end{bmatrix} \Leftarrow \begin{bmatrix} \boxed{\mathbf{UD}} & \boxed{\mathbf{SD}} \\ \boxed{\mathbf{SD}} & \boxed{\mathbf{DD}} \end{bmatrix} \tag{11}$$

$$\mathbf{T}_{\mathrm{CD}} = \underbrace{\begin{bmatrix} \boldsymbol{e}_n^+ \\ \boldsymbol{D}_n^T \end{bmatrix}}_{\substack{\textbf{Receiver}\\ \textbf{transformation}\\ \textbf{part}}} \otimes \underbrace{\begin{bmatrix} \boldsymbol{I}_f \otimes \boldsymbol{e}_m^+ \\ \boldsymbol{I}_f \otimes \boldsymbol{D}_m^T \end{bmatrix}}_{\substack{\textbf{Satellite}\\ \textbf{transformation}\\ \textbf{part}}}. \tag{12}$$

In (12), the left-hand side of the symbol $\otimes$ represents the transformation matrix related to the receiver components, with the subscript n indicating station-related terms. The right-hand side of the symbol $\otimes$ represents the transformation matrix concerning the satellite components, with the subscript m indicating satellite-related terms. $\boldsymbol{D}_n \in \mathbb{R}^{n\times(n-1)}$ and $\boldsymbol{D}_m \in \mathbb{R}^{m\times(m-1)}$ are the between-station and between-satellite differencing matrices, respectively, with the first station or the first satellite serving as the datum. $\boldsymbol{e}_n^+$ and $\boldsymbol{e}_m^+$ are the orthogonal vectors of $\boldsymbol{D}_n^T$ and $\boldsymbol{D}_m^T$, respectively, i.e., $\boldsymbol{D}_n^T\boldsymbol{e}_n^+ = \boldsymbol{0}$ and $\boldsymbol{D}_m^T\boldsymbol{e}_m^+ = \boldsymbol{0}$, where $\boldsymbol{e}_n^+$ and $\boldsymbol{e}_m^+$ are expressed as

$$\boldsymbol{e}_n^+ = \frac{\boldsymbol{e}_n^T\boldsymbol{C}_R^{-1}}{\boldsymbol{e}_n^T\boldsymbol{C}_R^{-1}\boldsymbol{e}_n}, \quad \boldsymbol{e}_m^+ = \frac{\boldsymbol{e}_m^T\boldsymbol{C}_S^{-1}}{\boldsymbol{e}_m^T\boldsymbol{C}_S^{-1}\boldsymbol{e}_m}. \tag{13}$$

B. Impact of IAR on Atmospheric Parameters

In contrast to [48], the use of SCE model is restricted to obtaining only ionospheric slant delays and cannot directly

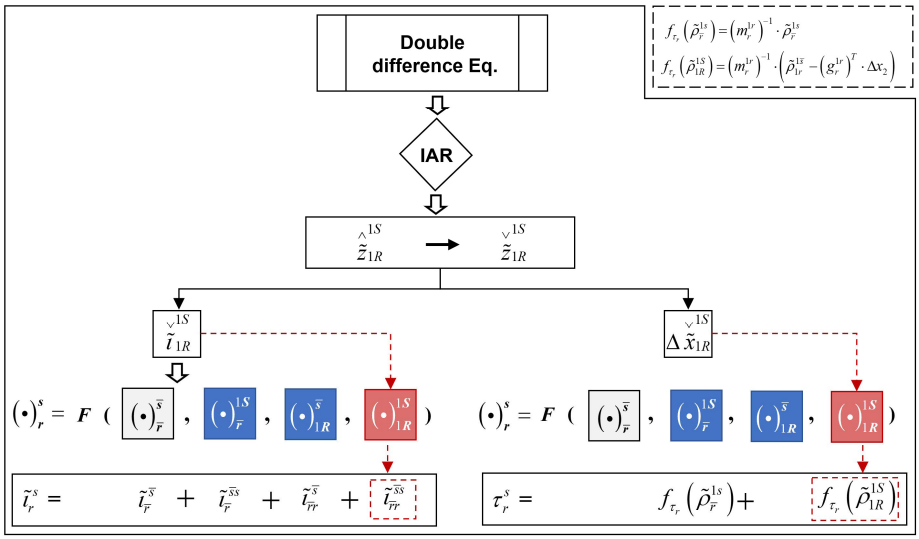

Fig. 3. Improvements in atmospheric parameter estimation after fixing DD ambiguities.

estimate single-station ZTD. To overcome this limitation, we extended the CD theory to the SCF model, enabling an exploration of the impact of IAR on the estimation of both ionospheric and tropospheric delays.

Based on the CD theory, any observation or parameter can be expressed as a function of the UD, SD, and DD blocks. Consequently, the ionospheric delay parameter can be conveniently reformulated in the form presented in the following equation:

$$\begin{aligned} \textbf{Float solution: } \hat{\tilde{\imath}}_r^s &= \hat{\tilde{\imath}}_{\bar{r}}^{\bar{s}} + \hat{\tilde{\imath}}_{\bar{r}}^{\bar{s}s} + \hat{\tilde{\imath}}_{\bar{r}r}^{\bar{s}} + \hat{\tilde{\imath}}_{\bar{r}r}^{\bar{s}s} \\ \textbf{Fixed solution: } \check{\tilde{\imath}}_r^s &= \check{\tilde{\imath}}_{\bar{r}}^{\bar{s}} + \check{\tilde{\imath}}_{\bar{r}}^{\bar{s}s} + \check{\tilde{\imath}}_{\bar{r}r}^{\bar{s}} + \check{\tilde{\imath}}_{\bar{r}r}^{\bar{s}s} \end{aligned} \tag{14}$$

where the superscript $(\wedge)$ denotes the estimated float solution, while the superscript $(\vee)$ denotes the estimated fixed solution. $\hat{\tilde{\imath}}_{\bar{r}}^{\bar{s}s}$, $\hat{\tilde{\imath}}_{\bar{r}r}^{\bar{s}}$, and $\hat{\tilde{\imath}}_{\bar{r}r}^{\bar{s}s}$ are functions of the between-satellite SD $\tilde{\imath}_{\bar{r}}^{1S}$, between-station SD $\tilde{\imath}_{1R}^{\bar{s}}$, and DD $\tilde{\imath}_{1S}^{1R}$ components, respectively. From the perspective of the estimable parameter forms and the impact of IAR on the ionosphere, two conclusions can be easily drawn.

1) Combining the expression $\tilde{I}_r^s = I_r^s + d_{r,\mathrm{GF}} - d_{,\mathrm{GF}}^s$ for UD ionospheric estimation in Table I and (14), it can be seen that the UD ionospheric delay estimation is biased with the satellites and receivers' DCB parameters. Additionally, the ionospheric slant delay in both single-difference forms still contains DCB parameters, which means that code observation data are required for parameter estimation.
2) As shown in the decomposition expressions on the right of Fig. 3, the precision gain from IAR for the ionospheric delay is obtained only from the DD component. In the DD observation equation, after IAR, the DD ambiguity parameters with integer characteristics can move to the left-hand side of the equation. This effectively increases the observation precision by two orders of magnitude, bringing it to the level of precision of phase observations. Since the UD and SD components do not benefit from IAR, the precision of these components cannot be further improved.

In the A-PADD model, stations are distributed within a micronetwork, meaning that the ionospheric delays observed by each station for the same satellite are nearly identical, i.e., $\tilde{\imath}_{1r}^s = 0$, and furthermore, one can get $\tilde{\imath}_{1r}^{1s} = \tilde{\imath}_{1r}^s - \tilde{\imath}_{1r}^1 = 0$ [40], [47]. The decomposition of the ionospheric delay thus changes to the form in (15). This implies that IAR will not affect the estimation of ionospheric parameters. In this case, the accuracy improvement of A-PADD over UCPPP is attributed to the increase in redundant observations and enhanced model strength. The improvements in atmospheric parameter estimation after fixing DD ambiguities are illustrated in Fig. 3, which is based on the approach developed in [48]

$$\check{\tilde{\imath}}_r^s = \check{\tilde{\imath}}_{\bar{r}}^{\bar{s}} + \check{\tilde{\imath}}_{\bar{r}}^{\bar{s}s} + \check{\tilde{\imath}}_{\bar{r}r}^{\bar{s}} + 0. \tag{15}$$

The tropospheric delay is a nondispersive error and part of the geometric term. Therefore, after fixing the DD ambiguities, the expression for tropospheric delay can be rewritten, as shown in Fig. 3. As depicted in the figure, the tropospheric delay can be affected through the geometric distance correction term in its DD form.

IV. Experiment Results and Analysis

This section validates the proposed method. We begin by describing the experimental setup, detailing the data collection and processing strategies.

To evaluate the performance of atmospheric delay determination, we selected specific test stations within the IGS network that meet the colocation criteria. We analyzed the impact of IAR on the extracted atmospheric delays and compared the performance of UCPPP and A-PADD in atmospheric parameter determination.

A. GNSS Data Collection and Processing Strategies

Within the IGS network, 12 pairs of stations distributed globally were selected for the experiment, as shown in Fig. 4.

To ensure consistency across the test stations, the dataset for the experiment consisted solely of GPS dual-frequency

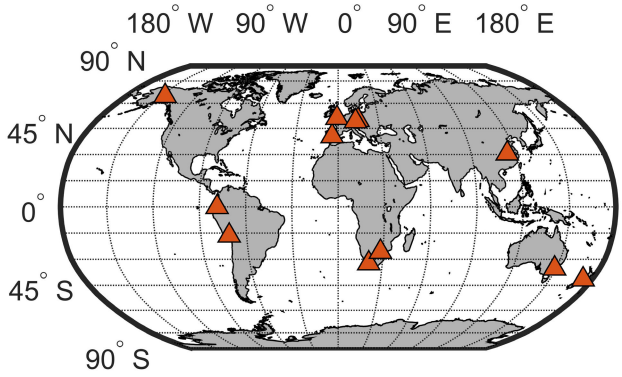

Fig. 4. Location of the 12 pairs of stations selected from the IGS network for the experiment.

code and phase observations. The observation period was on DOY 092 of 2023, with a sampling interval of 30 s. The main data processing strategies are shown in Table III. During data processing, a Kalman filter was used as the parameter estimator, with IAR achieved using the least-squares ambiguity decorrelation adjustment (LAMBDA) method. A bootstrapped success rate threshold of 99.99% was applied to fix the ambiguities to integers. While the Kalman filter is a widely adopted method in GNSS data processing, recent studies have proposed factor graph optimization methods [50], which may provide enhanced robustness for future research.

B. Impact of IAR on Atmospheric Delay Determination in A-PADD Method

In Section III, the impact of IAR on ionospheric and tropospheric parameters was presented analytically. In this section, we will analyze the effects on these parameters before and after IAR using a real GNSS dataset. The concept of the gain number [51] is utilized to characterize changes in the accuracy of the estimated parameters due to IAR. First, the expression for the gain number is expressed as

$$\gamma(l) = \frac{l^T Q_{\hat{x}\hat{x}} l}{l^T Q_{\check{x}\check{x}} l} = 1 + \frac{l^T (Q_{\hat{x}\hat{x}} - Q_{\check{x}\check{x}}) l}{l^T Q_{\check{x}\check{x}} l} \tag{16}$$

where x represents the vector of parameters to be estimated, and the vector l with the value 1 at the positions corresponding to the parameters of interest, while all other entries are 0. $Q_{\hat{x}\hat{x}}$ and $Q_{\check{x}\check{x}}$ denote the variance–covariance matrices before and after ambiguity fixing, respectively. The gain number $\gamma(l)$ indicates how much the accuracy of the parameters of interest improves after ambiguity fixing. From (16), we can also see that the gain number is always greater than 1, indicating that successfully fixing the ambiguity does not decrease the accuracy.

Our motivation is to effectively utilize existing colocated CORS station data to improve the performance of atmospheric delay extraction through the A-PADD method, thereby demonstrating its feasibility and effectiveness. Since most colocated CORS stations are typically equipped with only two receivers, we focus on a two-receiver array-aided setup to analyze the atmospheric parameter extraction results of A-PADD and compare them with those obtained using the UCPPP method.

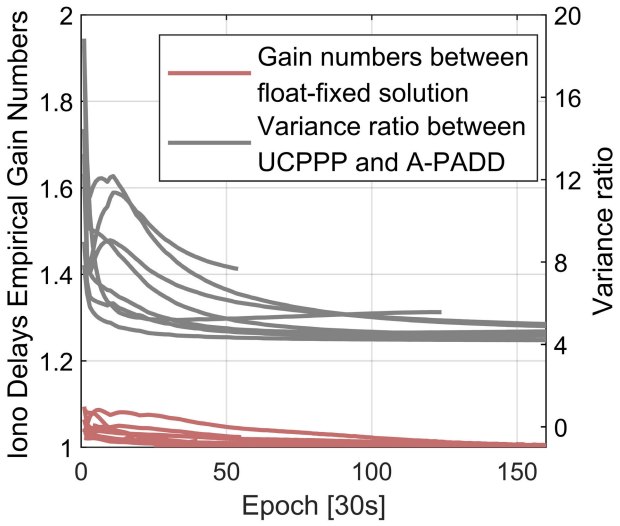

Fig. 5. Ionospheric delay empirical gain numbers and variance ratio between UCPPP and A-PADD.

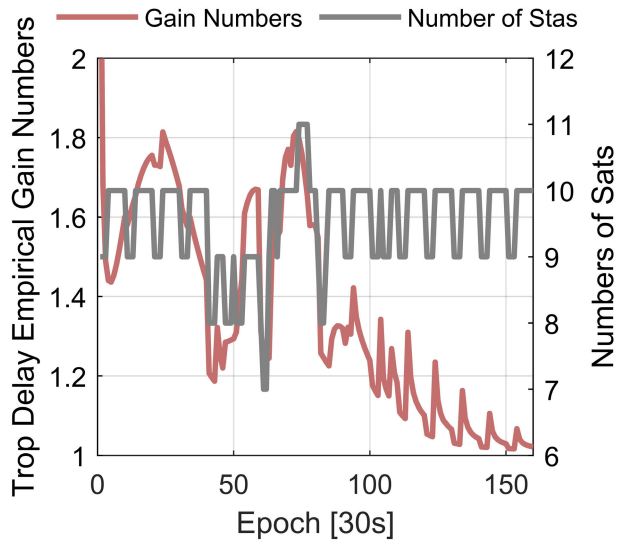

Fig. 6. Time series of the empirical gain number for tropospheric delay and the number of satellites.

Taking the SUTM station as an example, the ionospheric gain numbers and the variance ratio between UCPPP and A-PADD were plotted. The parameter processing strategy, consistent with that in Table III, treats the ionospheric parameters as white noise. The results are illustrated in Fig. 5.

In Fig. 5, the left vertical axis represents the gain numbers for ionospheric delay, with the red curve reflecting the accuracy change in the ionospheric parameters before and after achieving IAR for each satellite. The gain numbers consistently remain below 1.1 and are relatively stable, indicating that the difference between the float and fixed solutions is minimal, aligning with the theoretical results derived in Section III. The right vertical axis represents the post-variance ratio between UCPPP and A-PADD, with the gray curve illustrating the accuracy comparison for each satellite under the two methods. The initial large fluctuations in the variance ratio can be attributed to the greater number of redundant observations in A-PADD compared to UCPPP,

TABLE III
PROCESSING STRATEGIES USED IN A-PADD AND UCPPP

Items	Models/Strategies
Frequency	GPS L1 and L2
Estimator	Kalman filter
Elevation cutoff angle	7.5°
Weighting strategy	Elevation-dependent weighting For raw data: Code: $\sigma_p = 0.3m$ Phase: $\sigma_\phi = 0.003m$
Orbit and satellite clock	Precise orbit & Precise satellite clock
Receiver clock	Estimated as white noise
Slant ionospheric delays	Estimated as white noise
Zenith Tropospheric delay	Dry delay: provided by the UNB3m model [52] Wet delay: estimated as random-walk, with noise ($10^{-4} m/\sqrt{s}$) GMF is used for the mapping function [53]
Phase ambiguities	Estimated as float constants for each arc, fixing ambiguities per epoch
Between-receiver DCBs	Estimated as white noise
Between-satellite phase biases	Estimated as white noise
PCO and PCV correction	Corrected by .atx file

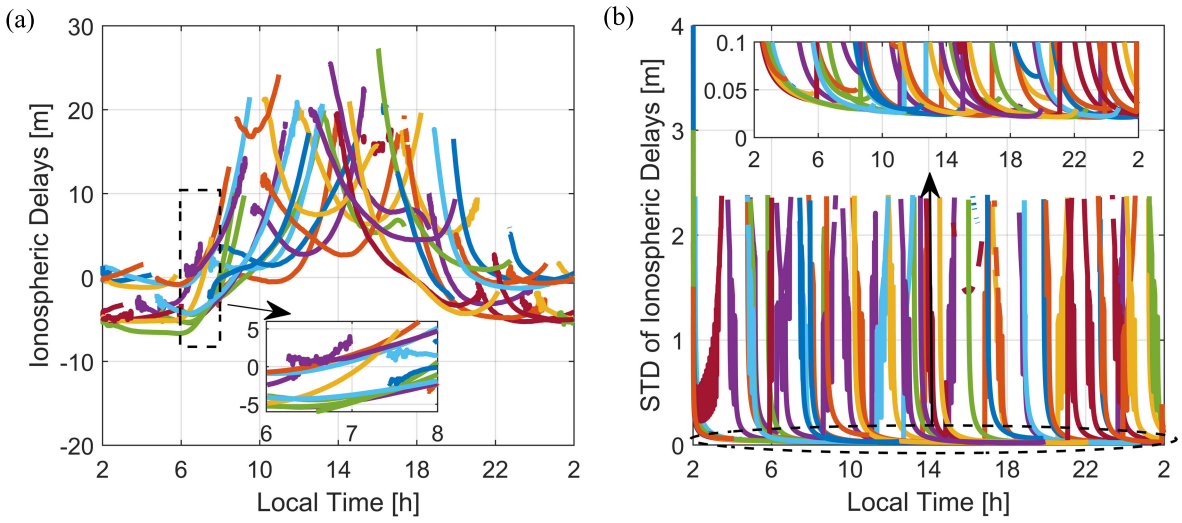

Fig. 7. Ionospheric slant delay time series at SUTM under UCPPP processing on DOY 092. (a) Time series of ionospheric delay. (b) STD of ionospheric delay.

resulting in a smaller and more stable initial variance. As the phase-related parameters gradually converge, the post-variance ratio between the two methods becomes stable. Fig. 5 also shows that A-PADD provides a significant improvement in the ionospheric extraction accuracy over UCPPP, particularly in the initial stages. Additionally, for users primarily concerned with ionospheric delay, it is possible to achieve a comparable level of accuracy without IAR.

In addition to evaluating the impact of IAR on ionospheric parameters, we also assessed its effect on tropospheric parameters. To better reflect the impact of ambiguity fixing on tropospheric parameters, the parameter processing strategy was slightly adjusted, where tropospheric parameters were treated as white noise.

In Fig. 6, the left vertical axis represents the tropospheric gain number, linked to the red curve in the figure. Initially, the empirical gain number is relatively high, but it decreases as the phase-related parameters converge over time, approaching "1" when the float and fixed solutions for ambiguity become nearly identical. Fig. 6 further demonstrates that variations in the number of satellites have a direct impact on the tropospheric gain number. Specifically, a decrease in the number of satellites leads to fewer observations and fixed ambiguities, lowering the gain number. This indicates

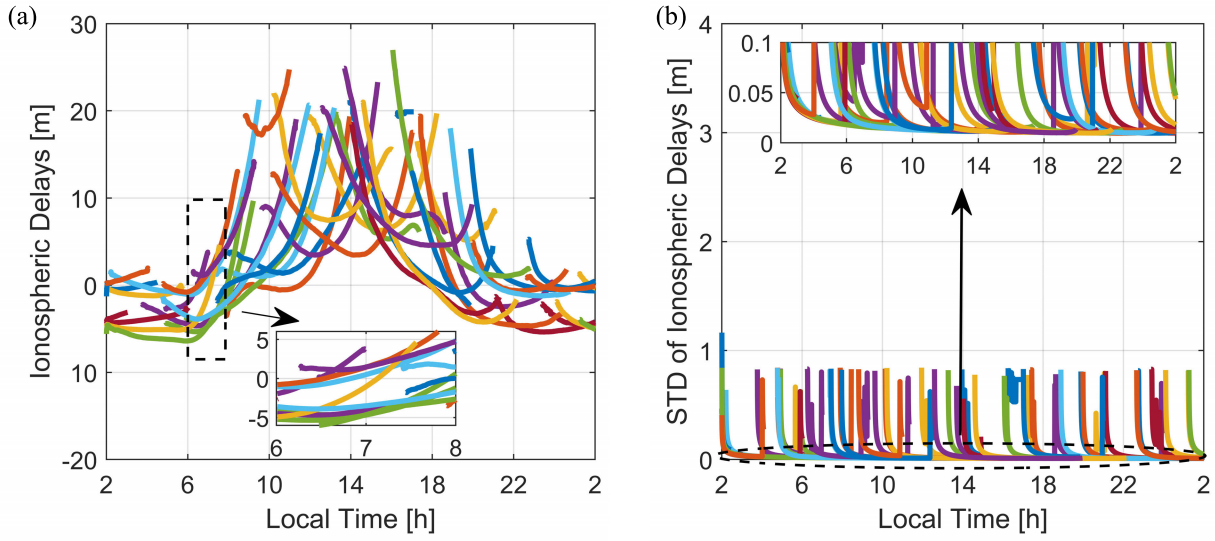

Fig. 8. Ionospheric slant delay time series at SUTM under A-PADD processing on DOY 092. (a) Time series of ionospheric delay. (b) STD of ionospheric delay.

a significant relationship between tropospheric gain numbers, satellite counts, and ambiguity-fixing status. Overall, this analysis highlights the effectiveness of implementing IAR for users concerned with estimation of both ionospheric and tropospheric delays, particularly during the initial stages of tropospheric parameter estimation.

C. Comparison of Ionospheric Delay Determination Performance Between UCPPP and A-PADD

We analyzed the performance improvement of A-PADD compared to UCPPP in determining the ionospheric delay, using the SUTM station as an example. Figs. 7 and 8 illustrate the time series of ionospheric delay (left panels) and the standard deviation (STD) of ionospheric delay (right panels) at SUTM for UCPPP and A-PADD processing modes, respectively.

The time series of the ionospheric delay reveals a clear diurnal variation pattern. As sunlight duration and intensity increase between local times 06:00 and 14:00, the electron density in the ionosphere gradually rises, leading to an increase in the ionospheric delay experienced by electromagnetic signals passing through the atmosphere. This delay peaks around local time 14:00 to 16:00 before gradually decreasing. Despite significant fluctuations in the ionospheric slant delay throughout the day, the overall trend in the time series extracted by both UCPPP and A-PADD remains consistent. This consistency is attributed to the similar parameter estimation methods employed in both processing modes, as the expression for ionospheric delay is identical in both methods, as demonstrated in (2)–(5). Essentially, A-PADD builds on the PPP framework and enhances traditional PPP by increasing redundant observations through observation stacking and integrating parameters in the parameter field, thereby strengthening the model.

However, diversity becomes apparent when examining the details. The subplots in Figs. 7(a) and 8(a), which zoom on the ionospheric delay time series between local times 06:00 and 08:00, reveal that the ionospheric delay

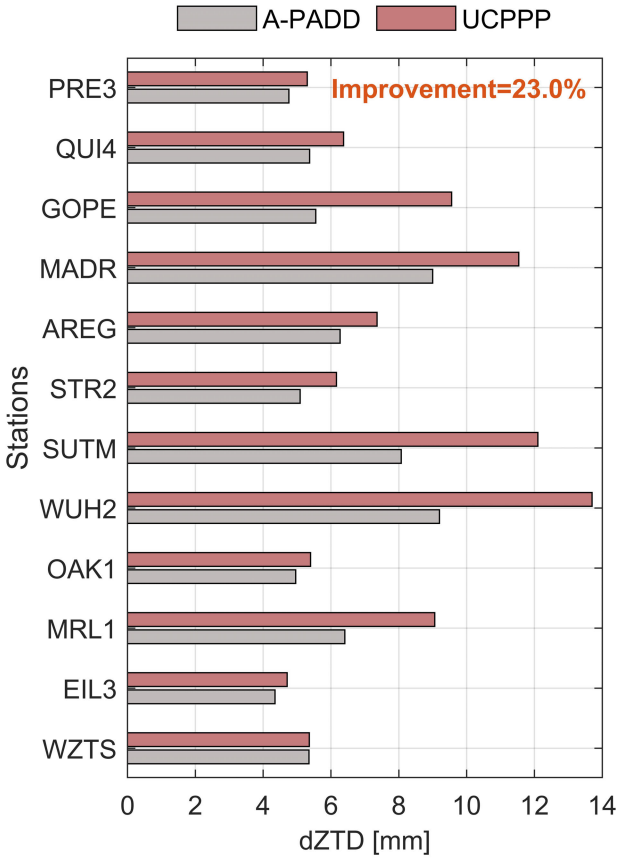

Fig. 9. Rms of dZTD in ZTD between A-PADD and UCPPP at each station.

extracted by UCPPP exhibits significant fluctuations, while the delay extracted by A-PADD is smoother and aligns more closely with the short-term variability characteristics of the ionosphere. These fluctuations typically occur as new satellites rise. The increased redundant observations and enhanced

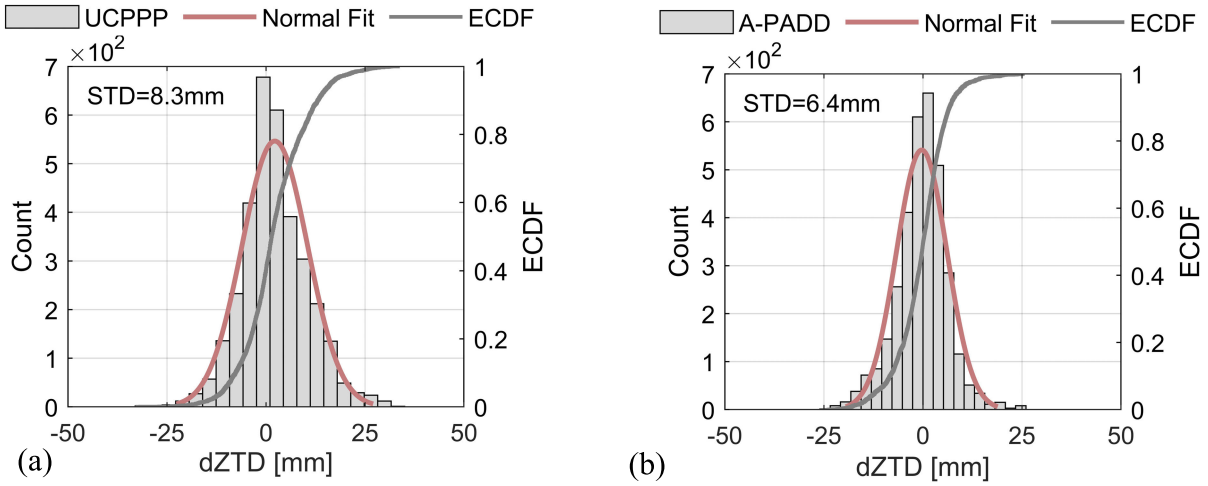

Fig. 10. Error distribution and ECDF of dZTD errors between UCPPP and A-PADD.

model strength in A-PADD contribute to a more efficient and accelerated initialization process for new satellites, resulting in more stable initial estimates of ionospheric delay.

Moreover, the STD of ionospheric delay estimated for UCPPP and A-PADD, as shown in Figs. 7(b) and 8(b), clearly highlights a noticeable difference between the two methods. With A-PADD, the initial STD of ionospheric delay decreases from above 2 (in UCPPP) to below 1. After the convergence of phase-related parameters, the STD in A-PADD remains at a lower level, theoretically providing more stable and accurate parameter inputs for ionospheric models such as GIM.

D. Comparison of Tropospheric Delay Determination Performance Between UCPPP and A-PADD

Next, we analyzed the tropospheric delay extraction using the 12 globally distributed station pairs. To evaluate the accuracy of tropospheric delay extraction with UCPPP and A-PADD, we selected the IGS final tropospheric product as a reference, which is available at https://cddis.nasa.gov/archive/gnss/products/troposphere/zpd/. The IGS associate analysis centers produce precise tropospheric products based on ground-based GNSS observations, utilizing IGS final orbit, satellite clock, and Earth orientation parameter (EOP) products. These data include ZTD as well as the north–south and east–west tropospheric gradient components, with a sampling interval of 5 min. To ensure consistency in sampling and accuracy for the comparison, only the epochs in the 30-s resolution results that coincided with the IGS final tropospheric product were selected for comparison, thereby avoiding accuracy loss due to interpolation.

Fig. 9 summarizes the tropospheric delay extraction results for the 12 globally distributed colocated stations. In Fig. 9, the vertical axis represents the rms of the difference in ZTD (dZTD) between the results obtained from A-PADD or UCPPP and the IGS final tropospheric product, with units in millimeters. The gray histogram represents the results from the A-PADD processing, while the red histogram represents the results from the UCPPP processing. As illustrated in Fig. 9, the rms of dZTD at each station decreases to some extent when using the A-PADD processing method, indicating better consistency with the IGS final tropospheric product and improved accuracy in tropospheric delay extraction. The differences in rms and accuracy improvement across stations may be attributed to various factors, including station location, observation quality, water vapor content, and the degree of atmospheric variability. Fig. 9 also demonstrates a 23% overall improvement in ZTD extraction with A-PADD.

To further evaluate the specific performance of both methods in terms of the distribution of ZTD errors, Fig. 10 presents the error distribution and empirical cumulative distribution function (ECDF) of dZTD errors for the UCPPP and A-PADD. Fig. 10(a) shows the dZTD error distribution for the UCPPP method, with an STD of 8.3 mm; Fig. 10(b) shows the dZTD error distribution for the A-PADD method, with an STD of 6.4 mm. The histograms represent the frequency distribution of errors, the red line indicates the normal fit curve, and the gray line represents the ECDF. In typical parameter estimation strategies, the ZTD parameter is often modeled as a random walk process. If there are no unmodeled errors are present and the associated noise is white noise, the ZTD error distribution should then follow a Gaussian distribution. As shown in Fig. 10, the error distribution of the ZTD for the A-PADD method is more concentrated with a mean close to zero and is closer to a normal distribution, indicating superior consistency with the IGS final products. In contrast, the UCPPP method shows a more spread error distribution and a larger STD, indicating greater error fluctuations and relatively lower stability. Comparing the ECDF of the two methods highlights the advantage of A-PADD in terms of cumulative error probability. The ECDF curve for the A-PADD method is steeper, indicating that most errors are concentrated within a smaller range, while the ECDF curve for the UCPPP method is flatter, showing a wider error range.

To evaluate the specific performance improvements of the A-PADD and UCPPP methods at different GNSS stations more comprehensively, Fig. 11 presents the tropospheric delay error distribution and its rms for the 12 test GNSS stations. In Fig. 11, the red lines and text represent the error distribution

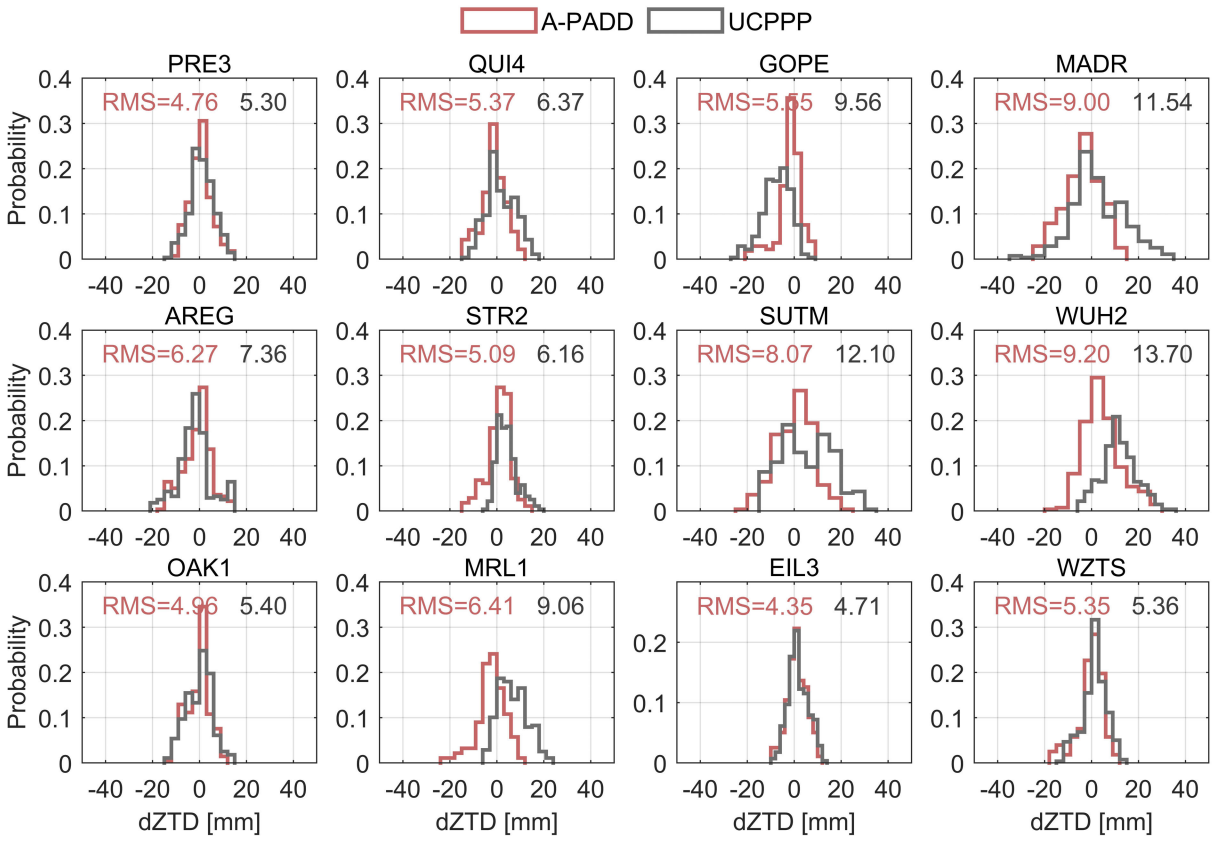

Fig. 11. Error distribution and ECDF of dZTD errors between UCPPP and A-PADD.

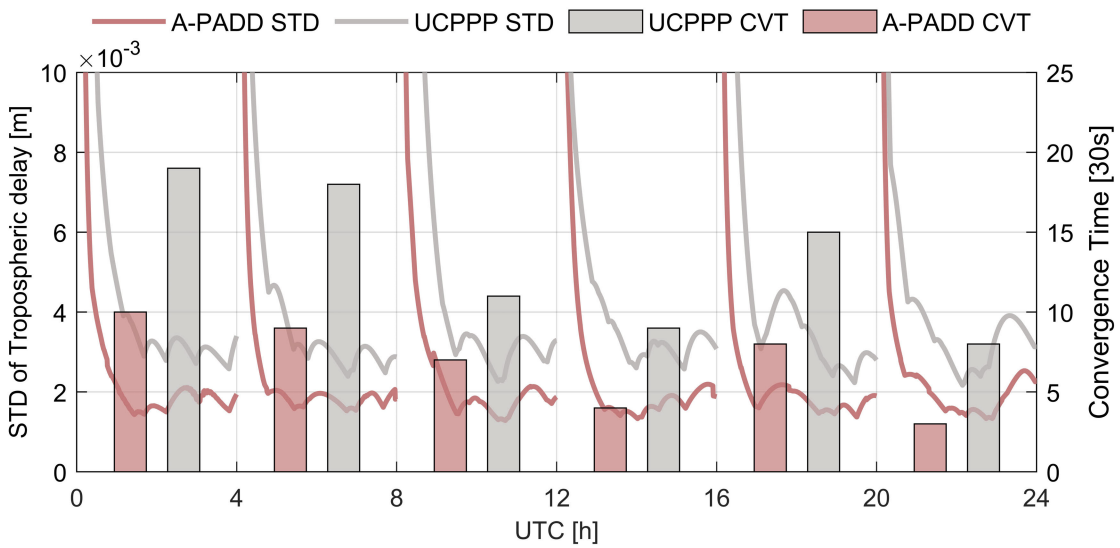

Fig. 12. Error distribution and ECDF of dZTD errors between UCPPP and A-PADD.

and rms of A-PADD, while the gray lines and text represent those of UCPPP. A comparison clearly shows that A-PADD exhibits a mean closer to zero and more concentrated errors at each station, indicating better performance at all stations.

Additionally, taking the SUTM station as an example, we analyzed the initialization behavior of A-PADD and UCPPP in tropospheric delay extraction. Fig. 12 shows the time series of STD of tropospheric delay and a comparison of the first CVT between the A-PADD and UCPPP methods. During data processing, reinitialization was performed every 4 h, and the convergence criterion for tropospheric delay was defined as the time at which the difference between the estimated ZTD and the tropospheric product at the same epoch remains continuously less than 1 cm.

In Fig. 12, the red line represents the STD of tropospheric delay extraction using the A-PADD method, while the gray line represents the STD using the UCPPP method. During each initialization, the STD of the A-PADD method quickly

decreases and remains at a lower level, significantly below that of the UCPPP method, indicating superior performance in tropospheric delay estimation. After convergence, the variance trends of both the A-PADD and UCPPP methods are similar. The red bars in Fig. 12 represent the first CVT of the A-PADD method, while the gray bars represent the first CVT of the UCPPP method. The CVT of the A-PADD method is generally shorter than that of the UCPPP method, indicating that A-PADD can reach a stable state more quickly, providing more timely tropospheric delay estimation results. This analysis of STD and CVT shows that the A-PADD method offers higher accuracy and faster convergence in tropospheric delay estimation, making it capable of providing more precise and reliable tropospheric delay estimates in practical applications.

V. Conclusion

Ground-based GNSS observations are crucial for obtaining high-resolution ionospheric and tropospheric data, making them essential for space weather monitoring. Their high temporal and spatial resolution have led to extensive applications across various scientific disciplines. Nevertheless, the commonly used single-station PPP technique suffers from accuracy limitations due to excessive parameter estimation, external interference, and float ambiguities solution. Array-aided GNSS provides a potential solution to these challenges. Unlike traditional array-aided models that use the SCE model, which cannot directly provide single-station ZTD, this study introduces the SCF model in an array-aided setup scenario. This approach simultaneously estimates ionospheric and tropospheric delays with IAR from colocated GNSS stations, utilizing the spatial distribution characteristics of atmospheric delays. By reprocessing the ionospheric and tropospheric delays along with ambiguity parameters and increasing redundant observations, the model's robustness is enhanced, observational noise is reduced, and rapid IAR is achieved.

We further extended the CD theory from the SCE model to the SCF model to partition atmospheric parameters and conducted a theoretical analysis of the impact of IAR. Fixing DD ambiguities primarily enhances the DD components following the CD theory. For the frequency-dependent ionospheric delay, the benefit from a fixed solution is determined by the magnitude of the DD ionospheric delay. Given the short distances between colocated reference stations, the DD ionospheric delay is nearly zero, making the impact of IAR on ionospheric delay negligible. Experimental results support this theory. In contrast, for the tropospheric delay, a geometric term, IAR does yield some improvement. However, due to the proximity of the stations, the ambiguity parameters tend to converge to near-integer values over time, allowing accuracy levels similar to those of the fixed solution. Consequently, the gain in tropospheric delay diminishes as the filtering time increases.

We tested 12 pairs of IGS colocated stations and compared the extracted atmospheric delays with those obtained using the UCPPP method. In the comparison of atmospheric delay extraction performance, the A-PADD method demonstrated superior extraction accuracy and greater stability. The increase in redundant observations enhances the model strength for parameter estimation, allowing the A-PADD method to accelerate the initialization process of new satellites, resulting in a more rapid reduction in variance and lower STDs. Moreover, A-PADD avoids the significant fluctuations in ionospheric delay extraction that occur during the early rise of new satellites in the UCPPP method. For the tropospheric delay extraction, A-PADD improves the extraction accuracy by 23% compared to UCPPP. Regarding error distribution characteristics, the errors in the A-PADD method are more concentrated, with a mean close to zero and a distribution that more closely follows a normal distribution, indicating better consistency with the IGS final products in ZTD.

In summary, IAR does not provide significant gains in ionospheric delay estimation with in an array-aided GNSS setup. For applications solely interested in the ionospheric delay, it is possible to achieve accuracy similar to the fixed solution without ambiguity fixing, thereby reducing the required computational load. However, for users interested in both ionospheric and tropospheric delays, IAR provides some gains during the initialization stage of tropospheric delay estimation, making it the preferable method. In this study, we used postprocessing products released by IGS. In future research, we will further investigate array-aided precise ionospheric and tropospheric delay determination methods using precise products from satellite-based augmentation systems, such as BDS PPP-B2b, Galileo HAS, and QZSS MADOCA [54], [55], [56], [57].

Acknowledgment

The authors would like to thank the International GNSS Service (IGS) and the Crustal Dynamics Data Information System (CDDIS), for providing the GNSS data support.

References

[1] N. Jakowski, "Ionosphere monitoring," in *Springer Handbook of Global Navigation Satellite Systems*. cham, Switzerland: Springer, 2017, pp. 1139–1162, doi: 10.1007/978-3-319-42928-1_39.

[2] Y. Yasyukevich, E. Astafyeva, A. Padokhin, V. Ivanova, S. Syrovatskii, and A. Podlesnyi, "The 6 September 2017 X-sclass solar flares and their impacts on the ionosphere, GNSS, and HF radio wave propagation," *Space Weather*, vol. 16, no. 8, pp. 1013–1027, Aug. 2018, doi: 10.1029/2018sw001932.

[3] C. López-Urias, G. E. Vazquez-Becerra, K. Nayak, and R. López-Montes, "Analysis of ionospheric disturbances during X-class solar flares (2021–2022) using GNSS data and wavelet analysis," *Remote Sens.*, vol. 15, no. 18, p. 4626, Sep. 2023.

[4] Y. Yuan, N. Wang, Z. Li, and X. Huo, "The BeiDou global broadcast ionospheric delay correction model (BDGIM) and its preliminary performance evaluation results," *Navigation*, vol. 66, no. 1, pp. 55–69, Jan. 2019, doi: 10.1002/navi.292.

[5] R. Prieto-Cerdeira, R. Orús-Pérez, E. Breeuwer, R. Lucas-Rodriguez, and M. Falcone, "Performance of the Galileo single-frequency ionospheric correction during in-orbit validation," *GPS World*, vol. 25, no. 6, pp. 53–58, 2014.

[6] J. A. Klobuchar, "Ionospheric time-delay algorithm for single-frequency GPS users," *IEEE Trans. Aerosp. Electron. Syst.*, vol. AES-23, no. 3, pp. 325–331, May 1987.

[7] G. Molera Calvés et al., "Analysis of an interplanetary coronal mass ejection by a spacecraft radio signal: A case study," *Space Weather*, vol. 15, no. 11, pp. 1523–1534, Nov. 2017, doi: 10.1002/2017sw001701.

[8] A. Krypiak-Gregorczyk, "Ionosphere response to three extreme events occurring near spring equinox in 2012, 2013 and 2015, observed by regional GNSS-TEC model," *J. Geodesy*, vol. 93, no. 7, pp. 931–951, Jul. 2019, doi: 10.1007/s00190-018-1216-1.

[9] T. Hobiger and N. Jakowski, "Atmospheric signal propagation," in *Springer Handbook of Global Navigation Satellite Systems*, vol. 6, no. 1. Cham, Switzerland: Springer, 2017, pp. 165–193, doi: 10.1007/978-3-319-42928-1_6.

[10] W. Rohm, Y. Yuan, B. Biadeglgne, K. Zhang, and J. L. Marshall, "Ground-based GNSS ZTD/IWV estimation system for numerical weather prediction in challenging weather conditions," *Atmos. Res.*, vol. 138, pp. 414–426, Mar. 2014.

[11] K. Wilgan, W. Rohm, and J. Bosy, "Multi-observation meteorological and GNSS data comparison with numerical weather prediction model," *Atmos. Res.*, vol. 156, pp. 29–42, Apr. 2015.

[12] K. Wilgan, G. Dick, F. Zus, and J. Wickert, "Tropospheric parameters from multi-GNSS and numerical weather models: Case study of severe precipitation and flooding in Germany in July 2021," *GPS Solutions*, vol. 27, no. 1, p. 49, Jan. 2023, doi: 10.1007/s10291-022-01379-0.

[13] J. M. Dow, R. Neilan, and C. Rizos, "The international GNSS service in a changing landscape of global navigation satellite systems," *J. Geodesy*, vol. 83, nos. 3–4, pp. 191–198, Mar. 2009, doi: 10.1007/s00190-008-0300-3.

[14] H. Zhang, Y. Yuan, W. Li, and B. Zhang, "A real-time precipitable water vapor monitoring system using the national GNSS network of China: Method and preliminary results," *IEEE J. Sel. Topics Appl. Earth Observ. Remote Sens.*, vol. 12, no. 5, pp. 1587–1598, May 2019, doi: 10.1109/JSTARS.2019.2906950.

[15] W. Zhang, S. Zhang, N. Ding, L. Holden, X. Wang, and N. Zheng, "GNSS-RS tomography: Retrieval of tropospheric water vapor fields using GNSS and RS observations," *IEEE Trans. Geosci. Remote Sens.*, vol. 60, 2022, Art. no. 4102313.

[16] C.-S. Huang, J. C. Foster, L. P. Goncharenko, P. J. Erickson, W. Rideout, and A. J. Coster, "A strong positive phase of ionospheric storms observed by the millstone Hill incoherent scatter radar and global GPS network," *J. Geophys. Res., Space Phys.*, vol. 110, no. A6, Jun. 2005, Art. no. 2004JA010865, doi: 10.1029/2004ja010865.

[17] S. Todorova, T. Hobiger, and H. Schuh, "Using the global navigation satellite system and satellite altimetry for combined global ionosphere maps," *Adv. Space Res.*, vol. 42, no. 4, pp. 727–736, Aug. 2008.

[18] M. J. Fernandes, C. Lazaro, A. L. Nunes, N. Pires, L. Bastos, and V. B. Mendes, "GNSS-derived path delay: An approach to compute the wet tropospheric correction for coastal altimetry," *IEEE Geosci. Remote Sens. Lett.*, vol. 7, no. 3, pp. 596–600, Jul. 2010.

[19] J. Bosy, W. Rohm, J. Sierny, and J. Kaplon, "GNSS meteorology," *TransNav-Int, J. Mar. Navig., Saf. Sea Transp.*, vol. 2011, pp. 79–83, May 2011.

[20] W. Zaw, Y. Goto, and Y. Kasahara, "Estimation method of ionospheric TEC distribution using single frequency measurements of GPS signals," *Int. J. Adv. Comput. Sci. Appl.*, vol. 7, no. 12, pp. 104–106, 2016.

[21] J. Jones et al., *Adv. GNSS Tropospheric Products for Monitor. Severe Weather Events Climate: COST Action ES1206 Final Action Dissemination Rep.* Cham, Switzerland: Springer, 2020, doi: 10.1007/978-3-030-13901-8.

[22] G. K. Seemala, "Estimation of ionospheric total electron content (TEC) from GNSS observations," in *Atmospheric Remote Sensing*. Amsterdam, The Netherlands: Elsevier, 2023, pp. 63–84.

[23] X. Li et al., "Retrieving of atmospheric parameters from multi-GNSS in real time: Validation with water vapor radiometer and numerical weather model," *J. Geophys. Res., Atmos.*, vol. 120, no. 14, pp. 7189–7204, Jul. 2015, doi: 10.1002/2015jd023454.

[24] B. Zhang, J. Ou, Y. Yuan, and Z. Li, "Calibration of slant total electron content and satellite-receiver's differential code biases with uncombined precise point positioning technique," *Acta Geod. Cartogr. Sin.*, vol. 40, no. 4, pp. 447–453, 2011.

[25] B. Zhang et al., "Determination of ionospheric observables with precise point positioning," *Chin. J. Geophy.*, vol. 54, no. 4, pp. 950–957, Apr. 2011.

[26] J. A. Lázaro, "Gnss array-based acquisition: Theory and implementation," Ph.D. dissertation, Dept. Signal Theory Communi., Universitat Politecnica de Catalunya, Barcelona, Spain, Jul. 2012.

[27] W. Nie et al., "The impacts of the ionospheric observable and mathematical model on the global ionosphere model," *Remote Sens.*, vol. 10, no. 2, p. 169, Jan. 2018.

[28] I. Herrera Pinzón and M. Rothacher, "Assessment of local GNSS baselines at co-location sites," *J. Geodesy*, vol. 92, no. 9, pp. 1079–1095, Sep. 2018, doi: 10.1007/s00190-017-1108-9.

[29] P. J. G. Teunissen, "A-PPP: Array-aided precise point positioning with global navigation satellite systems," *IEEE Trans. Signal Process.*, vol. 60, no. 6, pp. 2870–2881, Jun. 2012, doi: 10.1109/TSP.2012.2189854.

[30] B. Li and P. J. G. Teunissen, "GNSS antenna array-aided CORS ambiguity resolution," *J. Geodesy*, vol. 88, no. 4, pp. 363–376, Apr. 2014, doi: 10.1007/s00190-013-0688-2.

[31] A. Allahvirdi-Zadeh and A. El-Mowafy, "Array-aided precise orbit and attitude determination of CubeSats using GNSS," *NAVIGATION, J. Inst. Navigat.*, vol. 71, no. 3, Sep. 2024, Art. no. navi.651. [Online]. Available: https://doi.org/10.33012/navi.651

[32] X. An et al., "Undifferenced array PPP: A model for GNSS integrated positioning and attitude determination," *GPS Solutions*, vol. 28, no. 4, p. 213, Oct. 2024, doi: 10.1007/s10291-024-01755-y.

[33] J. Arribas, C. Fernandez-Prades, and P. Closas, "Antenna array based GNSS signal acquisition for interference mitigation," *IEEE Trans. Aerosp. Electron. Syst.*, vol. 49, no. 1, pp. 223–243, Jan. 2013.

[34] N. Vagle, A. Broumandan, A. Jafarnia-Jahromi, and G. Lachapelle, "Performance analysis of GNSS multipath mitigation using antenna arrays," *J. Global Positioning Syst.*, vol. 14, no. 1, p. 4, Dec. 2016, doi: 10.1186/s41445-016-0004-6.

[35] Y. Hu, S. Bian, B. Li, and L. Zhou, "A novel array-based spoofing and jamming suppression method for GNSS receiver," *IEEE Sensors J.*, vol. 18, no. 7, pp. 2952–2958, Apr. 2018.

[36] S. Zaminpardaz, P. J. G. Teunissen, N. Nadarajah, and A. Khodabandeh, "GNSS array-based ionospheric spatial gradient monitoring: Precision and integrity analyses," in *Proc. I_{ON} Pacific PNT Meeting*, 2015, pp. 799–814.

[37] A. Khodabandeh and P. J. G. Teunissen, "Array-aided multifrequency GNSS ionospheric sensing: Estimability and precision analysis," *IEEE Trans. Geosci. Remote Sens.*, vol. 54, no. 10, pp. 5895–5913, Oct. 2016, doi: 10.1109/TGRS.2016.2574809.

[38] R. Wang, G. Marut, T. Hadaś, and T. Hobiger, "Improving GNSS meteorology by fusing measurements of several colocated receivers on the observation level," *IEEE J. Sel. Topics Appl. Earth Observ. Remote Sens.*, vol. 17, pp. 7841–7851, 2024, doi: 10.1109/JSTARS.2024.3381792.

[39] X. Mi, B. Zhang, A. El-Mowafy, K. Wang, and Y. Yuan, "On the potential of undifferenced and uncombined GNSS time and frequency transfer with integer ambiguity resolution and satellite clocks estimated," *GPS Solutions*, vol. 27, no. 1, p. 25, Jan. 2023, doi: 10.1007/s10291-022-01363-8.

[40] X. Mi, B. Zhang, A. El-Mowafy, K. Wang, and Y. Yuan, "Undifferenced and uncombined GNSS time and frequency transfer with integer ambiguity resolution," *J. Geodesy*, vol. 97, no. 2, p. 13, Feb. 2023, doi: 10.1007/s00190-022-01689-8.

[41] P. J. G. Teunissen and O. Montenbruck, *Springer Handbook of Global Navigation Satellite Systems*. Cham, Switzerland: Springer, 2017, doi: 10.1007/978-3-319-42928-1.

[42] B. Zhang, P. Hou, J. Zha, and T. Liu, "PPP-RTK functional models formulated with undifferenced and uncombined GNSS observations," *Satell. Navigat.*, vol. 3, no. 1, p. 3, Feb. 2022, doi: 10.1186/s43020-022-00064-4.

[43] P. Hou, B. Zhang, and Y. V. Yasyukevich, "Homogeneous PPP-RTK user positioning performance as a consequence of network integer ambiguity resolution," *GPS Solutions*, vol. 28, no. 2, p. 60, Jan. 2024, doi: 10.1007/s10291-023-01600-8.

[44] P. Teunissen, "Zero order design: Generalized inverses, adjustment, the datum problem and S-transformations," in *Optimization and Design of Geodetic Networks*. Berlin, Germany: Springer, 1985, pp. 11–55, doi: 10.1007/978-3-642-70659-2_3.

[45] X. Mi, B. Zhang, and Y. Yuan, "Multi-GNSS RTK positioning with integer ambiguity resolution: From double-differenced to single-differenced," *J. Global Positioning Syst.*, vol. 17, no. 2, pp. 151–163, Dec. 2021, doi: 10.5081/jgps.17.2.151.

[46] T. Liu, Y. Yuan, B. Zhang, N. Wang, B. Tan, and Y. Chen, "Multi-GNSS precise point positioning (MGPPP) using raw observations," *J. Geodesy*, vol. 91, no. 3, pp. 253–268, 2017, doi: 10.1007/s00190-016-0960-3.

[47] D. Odijk, "Fast precise GPS positioning in the presence of ionospheric delays," Ph.D. dissertation, Delft Univ. Technol., Delft, Holland, 2002.

[48] A. Khodabandeh and P. J. G. Teunissen, "On the impact of GNSS ambiguity resolution: Geometry, ionosphere, time and biases," *J. Geodesy*, vol. 92, no. 6, pp. 637–658, Nov. 2017, doi: 10.1007/s00190-017-1084-0.

[49] P. J. G. Teunissen and A. Khodabandeh, "Do GNSS parameters always benefit from integer ambiguity resolution? A PPP-RTK network scenario," in *Proc. 27th Int. Tech. Meeting Satell. Division The Inst. Navigat. (ION GNSS+)*, 2014, pp. 590–600.

[50] G. Xiao et al., "PPP ambiguity resolution based on factor graph optimization," *GPS Solutions*, vol. 28, no. 4, p. 178, Aug. 2024, doi: 10.1007/s10291-024-01715-6.

[51] P. J. G. Teunissen, "A canonical theory for short GPS baselines," *J. Geodesy*, vol. 71, no. 7, pp. 389–401, Jun. 1997, doi: 10.1007/s001900050107.
[52] R. Leandro, M. C. Santos, and R. B. Langley, "UNB neutral atmosphere models: Development and performance," in *Proc. Nat. Tech. Meeting Inst. Navigat.*, Jan. 2006, pp. 564–573.
[53] J. Boehm, A. Niell, P. Tregoning, and H. Schuh, "Global mapping function (GMF): A new empirical mapping function based on numerical weather model data," *Geophys. Res. Lett.*, vol. 33, no. 7, Apr. 2006, Art. no. 2005GL025546, doi: 10.1029/2005gl025546.
[54] Y. Yang, Q. Ding, W. Gao, J. Li, Y. Xu, and B. Sun, "Principle and performance of BDSBAS and PPP-B2b of BDS-3," *Satell. Navigat.*, vol. 3, no. 1, p. 5, Dec. 2022, doi: 10.1186/s43020-022-00066-2.
[55] I. Fernandez-Hernandez et al., "Galileo high accuracy service: Initial definition and performance," *GPS Solut.*, vol. 26, p. 65, Jul. 2022, doi: 10.1007/s10291-022-01247-x.
[56] H. Namie and N. Kubo, "Performance evaluation of centimeter-level augmentation positioning L6-CLAS/MADOCA at the beginning of official operation of QZSS," *IEEJ J. Ind. Appl.*, vol. 10, no. 1, pp. 27–35, 2021.
[57] H. Wei, G. Xiao, P. Zhou, P. Li, Z. Xiao, and B. Zhang, "Combining Galileo HAS and beidou PPP-B2b with Helmert coordinate transformation method," *GPS Solutions*, vol. 29, no. 1, p. 35, Jan. 2025, doi: 10.1007/s10291-024-01789-2.

Xingyu Chen is currently pursuing the Ph.D. degree with the Innovation Academy for Precision Measurement Science and Technology, Chinese Academy of Sciences, Beijing, China.

He is a Research Assistant at the Department of Land Surveying and Geo-Informatics, The Hong Kong Polytechnic University, Hong Kong. His research interests include global navigation satellite system (GNSS) atmospheric monitoring and network RTK theory and applications.

Xiaolong Mi received the Ph.D. degrees from the University of Chinese Academy of Sciences, Beijing, China, in 2022, and Curtin University, Perth, WA, Australia, in 2023.

He is currently a Research Assistant Professor at the Department of Land Surveying and Geo-Informatics, The Hong Kong Polytechnic University, Hong Kong. His research interests include global navigation satellite system (GNSS) and low Earth orbit (LEO) technologies for positioning, navigation, and timing (PNT) along with the application of artificial intelligence (AI) in Earth and space sciences.

Yunbin Yuan is a Professor and the Director of the GNSS Application and Research Group, Innovation Academy for Precision Measurement Science and Technology, Chinese Academy of Sciences, Wuhan, China. His research interests include global navigation satellite system (GNSS)-based spatial environmental monitoring and analysis, high-precision GNSS satellite navigation and positioning, GNSS in orbit determination applications, and integrated navigation.

Ahmed El-Mowafy received the Ph.D. degree from the University of Calgary, Calgary, AB, Canada, in 1995.

He is currently a Professor and the Director of Graduate Research, School of Earth and Planetary Sciences, Curtin University, Perth, WA, Australia. He has more than 200 publications. His main research interests include precise positioning and navigation using global navigation satellite system (GNSS), quality control, POD, integrity monitoring, and estimation theory.

Hongjin Xu received the Ph.D. degree from the Innovation Academy for Precision Measurement Science and Technology (APM), Chinese Academy of Sciences (CAS), Wuhan, China, in 2024.

His research focuses on integrated navigation theory and applications.

Wenwu Ding received the Ph.D. degree from the Institute of Geodesy and Geophysics (IGG), Chinese Academy of Sciences (CAS), Wuhan, China, in 2013.

He is currently an Associate Professor with the Innovation Academy for Precision Measurement Science and Technology, CAS. His research interests focus on real-time satellite clock offset estimation.